Fabrication of High-Power Li-Ion Hybrid Supercapacitors by Enhancing the Exterior Surface Charge Storage

*Mei Yang, Yiren Zhong, Jingjing Ren, Xianlong Zhou, Jinping Wei, and Zhen Zhou**

Electrical energy-storage (EES) systems are anticipated to satisfy the increasing demand for large-scale applications with both high energy and large power requirements, e.g., in hybrid electric vehicles and electric vehicles.[1–3] Combining the complementary features of high-energy lithium-ion batteries (LIBs) and high-power capacitors, Li-ion hybrid electrochemical capacitors (Li-HECs) have become the focus of researchers for bridging the gap between LIBs and capacitors, with correspondingly different storage mechanisms at both ends, wherein LIB-type anodes establish large capacitances, and capacitor-type cathodes enable fast charge–discharge conditions.[4–6] Until now, several configurations have been realized for Li-HECs[7–10] of which the majority is composed of insertion-type anodes (such as $Li_4Ti_5O_{12}$, β-FeOOH, and TiO_2-B) and active carbon (AC) cathodes.[5,7,11]

However, for AC cathodes with merely electric double-layer capacitors (EDLCs) have unfavorable capacitance properties owing to the physical charge-storage mechanism.[12,13] Micropores constitute the majority in the pore structure, which further undermines the capacitive reaction at high-power conditions. Instead, heteroatom-functionalized carbon materials have been incorporated successfully to enhance the electrical conductivity and provide additional storage sites, highlighting reactive localized regions and variable electronic structures.[14,15] But it is of great importance to control the scales and pores to maximize interfacial reactions and ion transportation, because EDLCs and pseudocapacitors rely on surface-active phases.[16] Similarly, although possessing good structural robustness, insertion-type anodes are still hampered by low specific capacity, and can therefore not fully express the high-energy features of Li-HECs.[17–19] Metal oxides are considered preferable high-capacity substitutes, especially MnO.[20,21] Due to its attractive operation potential, i.e., below 0.5 V (vs. Li/Li^+), MnO is suitable for fabricating high-voltage Li-HECs in order to achieve a high energy–power combination. However, low conductivity, diffusion limitations, and large structural deviations have so far been major obstacles for its application in hybrid systems.

As a general rule for supercapacitor devices, the electrochemical performance needs to be confined to experimental timescales, i.e., on the order of minutes or seconds.[1,17] Nevertheless, for hybridized Li-HECs, the kinetics imbalance between the two ends impedes the full realization of the high power concept, leading to insufficient performance at high currents. In most cases, desirable energy storage (30–90 $Wh \cdot kg^{-1}$) can only be obtained at the expense of the power performance (<3 $kW \cdot kg^{-1}$),[5–7,19,22] which is far lower than the power performance targets required for new-generation electric vehicles (15 $kW \cdot kg^{-1}$).[18] Therefore, it will be a major challenge to design electrodes that can overcome the kinetics mismatch as well as achieve rapid electrochemical processes.[23] With larger external surface areas and shorter ion diffusion paths, various nanoarchitectures show an effective response to rapid redox reactions.[3,24] In particular, it was demonstrated that nanoscale architectures of less than 10 nm could enable pseudo-capacitance to overcome diffusion limitations for most reactions that occur at/near the surface.[25] Correspondingly, three-dimensional (3D) architectures with an interconnected carbon matrix render continuous and efficient electrical conductive networks with electron supplies that guarantee electrochemical reactions at high power.[26]

Here, we present high-power Li-ion hybrid supercapacitors (Li-HSCs) from the prospective of both single electrodes and devices, with two ends concurrently constructed with delicately engineered 3D hierarchical structures to overcome the kinetics discrepancy (**Figure 1**). A well-designed MnO–graphene composite (MnO@GNS) was devised as the anode with MnO nanocrystals (≈5 nm) homo-dispersed in the 3D architecture, while 3D hierarchical porous N-doped carbon (HNC) was used as the cathode with thin nanosheets forming the overall multi-porous framework. These scaffolds allow fast kinetics with ion diffusion paths narrowed down to ultrafine scales, as well as maximum exposure of the exterior surface. Both porous 3D electrodes with 2D ultrathin subunits facilitate high-power charge storage near the surface. The beneficial surface decoration of heteroatoms further improves the pseudo-capacitance performance of HNC, leading to higher capacitance than conventional carbon materials. As expected, the originally-devised hybrid Li–HSCs achieve attractive energy storage of 127 $Wh \cdot kg^{-1}_{electrodes}$, and even remains as high as 83.25 $Wh \cdot kg^{-1}$ at a battery-inaccessible power density of 25 $kW \cdot kg^{-1}$ with rapid charging within 8 s. Such a coherent design marks a new strategy for rationally fabricating hybrid devices with both high energy and power density by enhancing the exterior surface charge storage.

Dr. M. Yang, Y. R. Zhong, J. J. Ren, X. L. Zhou, Prof. J. P. Wei, Prof. Z. Zhou
Tianjin Key Laboratory of Metal and Molecule Based Material Chemistry
Key Laboratory of Advanced Energy Materials Chemistry (Ministry of Education)
Institute of New Energy Material Chemistry
School of Materials Science and Engineering
Collaborative Innovation Center of Chemical Science and Engineering (Tianjin)
Nankai University
Tianjin 300071, China
E-mail: zhouzhen@nankai.edu.cn

DOI: 10.1002/aenm.201500550

ADVANCED ENERGY MATERIALS
www.advenergymat.de

Materials Views
www.MaterialsViews.com

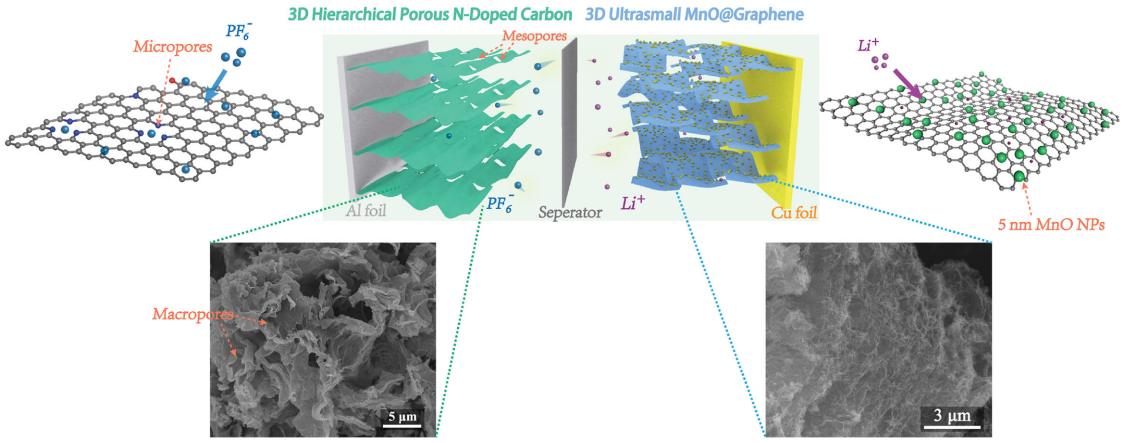

Figure 1. Illustration of Li-ion hybrid supercapacitors and corresponding SEM images of the electrode materials. The cathode employs 3D HNC materials and the anode utilizes prelithiated 3D MnO@GNS composites.

Material syntheses of both the cathode and anode materials were based on one-step routes followed by heat treatment without adding any hazardous or cost-ineffective materials. As shown in **Figure 2**a, the X-ray diffraction (XRD) patterns of MnO@GNS correspond to each crystal plane of MnO and a graphene (002) peak centered at ~24° (2θ). The utilization of Mn–organic complexes endows the composite with advantageous features with MnO robustly and uniformly interspersed on graphene matrix (Figure 2b), forming well-designed architectures at all dimensions (Figure S1, Supporting Information). The enlarged view in Figure 2c shows ultrafine MnO particles of about 5 nm, and these ultrasmall nanostructures could also be observed as broadened XRD peaks. Also, a representative three-layer thin graphene constituent was present in the supporting matrix with favorable conductivity, which was further verified by the low intensity ratio of I_D/I_G in the Raman spectrum (Figure S2, Supporting Information).[27]

The high-resolution X-ray photoelectron spectroscopy (XPS) measurements (Figure S3, Supporting Information) revealed the existence of Mn^{2+} while the C1s core level including C–O and C = O indicates the presence of oxygen residue; these species enable MnO particles to become strongly integrated on graphene.[28,29] Although MnO nanocrystals are abundantly integrated on graphene (67.4 wt% MnO, calculated from thermogravimetric-differential thermal analysis (TG-DTA, Figure S4, Supporting Information), the MnO@GNS composite

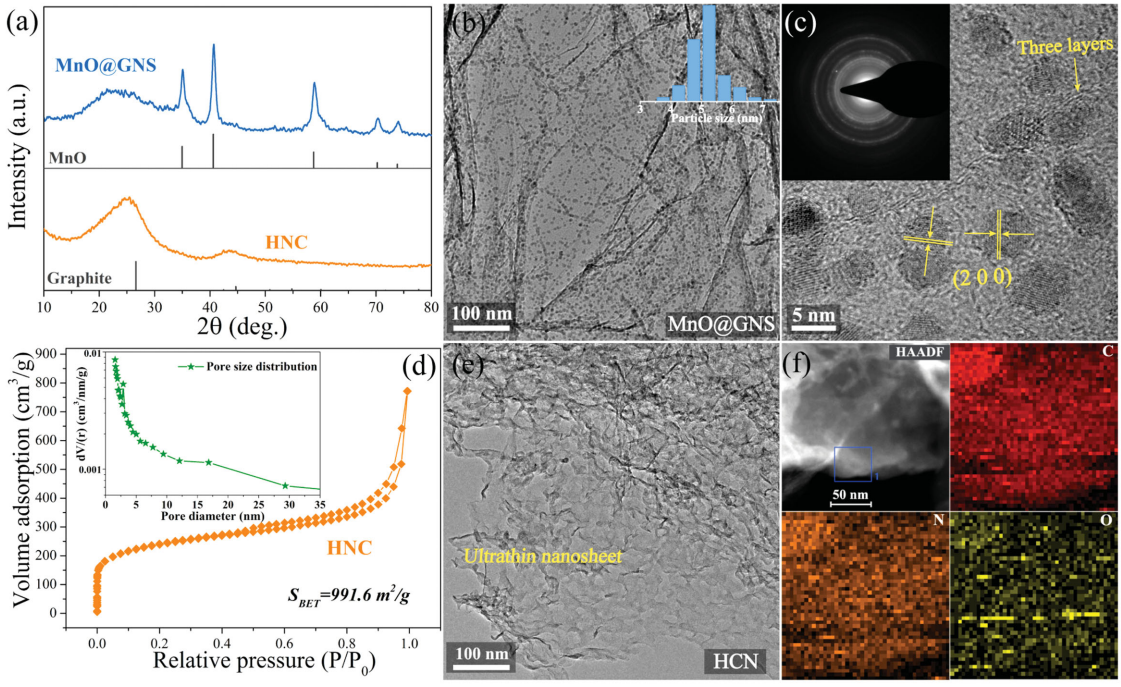

Figure 2. a) XRD patterns of related electrode materials. b,c) TEM images of MnO@GNS. d) N_2 adsorption–desorption isotherms. e) TEM image and f) corresponding element mapping of HNC.

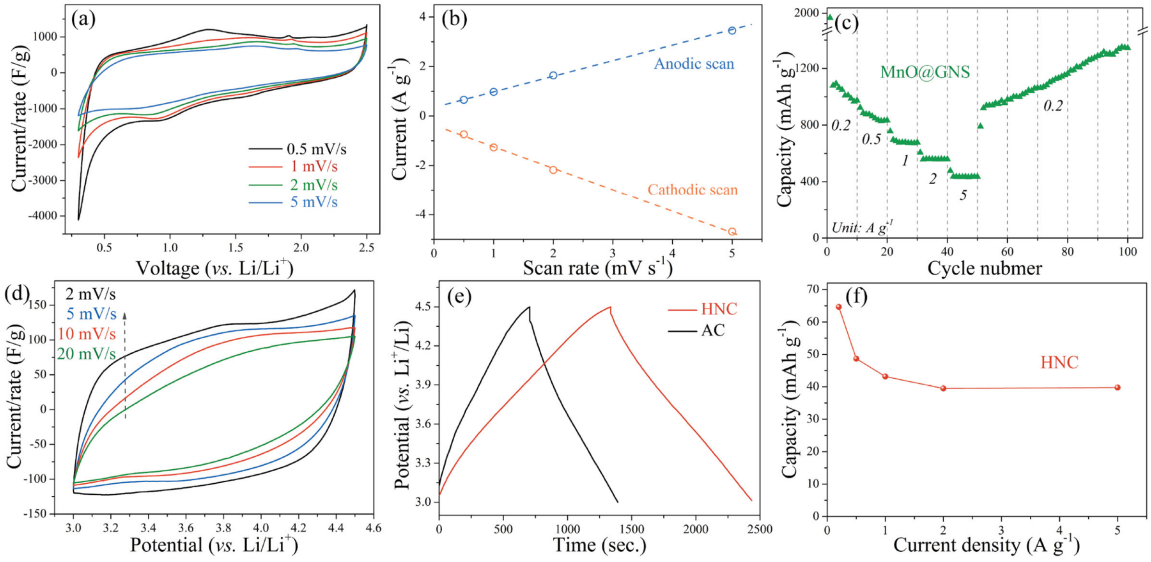

Figure 3. CV curves, charge–discharge plots and rate capability of MnO@GNS (a,c) and HNC (d,e,f), respectively. b) Correlation between the peak current and scan rate of MnO@GNS. e) Capacitance contrasts of HNC and AC at 0.2 A·g^{-1}. The CV current has been normalized by the scanning rate.

still manifests a high specific surface (162.6 m^2·g^{-1}) owing to the crimpled 3D architecture (Figure S5, Supporting Information).

The HNC shows a partially graphitic structure that corresponds to the (002) and (100) planes of graphite (Figure 2a). The low I_D/I_G ratio further implies highly graphitic features in the sp^2 domain (details in Figure S2, Supporting Information).[30,31] Owing to the bottom-up fabrication process accompanied by the gradual release of small molecules during pyrolysis, the HNC processes not only an intriguing porous structure ranging from micro- to macropores, but also fascinating chemical modification features with N- (5.12 wt%, elemental analysis) and O-functionalities on the carbon surface. The magnification image from one edge confirms an abundance of heteroatoms with a homogeneous distribution of each element (Figure 2f). The XPS in Figure S6 of the Supporting Information further elucidates the electronic structure of the core levels, with pyridinic N, pyrrolic N, quaternary N, and oxidized N as well as the –C=O and –C–O bond configuration for N1s and C1s, respectively, indicating the successful integration of these radicals.[32]

The transmission electron microscope (TEM) image in Figure 2e displays an ultrathin HNC transparent nanosheet with a graphene-like morphology, while the high-resolution TEM (HRTEM) image clearly shows a porous and graphitic structure (Figure S7, Supporting Information). As shown in Figure 2d, the N_2-adsorption curves can be classified as type I isotherms with a small type H4 hysteresis onset, which suggests that the structure combines many micropores, as well as meso- and macropores, which was further confirmed by the pore-size distribution plots shown in Figure 2d. The pore distribution results in a favorable Brunner–Emmet–Teller (BET) surface area (991.6 m^2·g^{-1}), especially for the high external surface (547.0 m^2·g^{-1}), which is much larger than that of micropore-dominated commercial AC (362.3 m^2·g^{-1}, Figure S8, Supporting Information).

The dark-field scanning TEM image (STEM, Figure S9, Supporting Information) shows that both electrode materials have curled frameworks with transparent textures. Combined with nanocrystals smaller than 10 nm and an ultrathin graphene/carbon matrix, such porous architectures expose a large fraction of the exterior interface of the active phase, which supports fast electrochemical charge storage as well as enhanced diffusion kinetics.[25,33,34]

First, half-cell assemblies were constructed to evaluate the electrochemical performance. **Figure 3**a shows cyclic voltammetry (CV) curves of the pre-lithiated MnO@GNS/Li configuration. Due to the nanometer-size features and enhanced exterior surface, the electrochemical behavior has quasi-pseudocapacitor characteristics similar to oxide/polymer supercapacitors in the range 0.3–2.5 V,[35–37] especially at larger scan rates. Except for a little polarization, further fitting clearly reveals a linear correlation between the peak current and sweep rate (Figure 3b),[39] indicating an effective circumvention of the diffusion-limited bulk electrochemical performance by confining most reactions to the surface.[34,38] Discharge–charge plots in Figure S10a of the Supporting Information confirm the low redox peaks (≈0.45 and 1.25 V), which are significant to construct high-voltage EES devices, especially for Li-HSCs utilizing asymmetric mechanisms at both ends. The hybrid shows high initial capacity over 1000 mAh·g^{-1} by taking advantage of ultrasmall MnO and the addition of graphene. Interestingly, the MnO@GNS electrode displays an ascending configuration, with a gradual increase to ≈1350 mAh·g^{-1} after 100 cycles (Figure 3c). This phenomenon is attributed to the readily re-oxidization of Mn^{II} to a higher valence state, which is confirmed by the common Mn-oxidization peak (≈2.1 V in CV) as well as with XPS and TEM measurements of the electrodes after several tens of cycles (Figure S11, Supporting Information).[21,38,39] Moreover, the composite delivers a high capacity of ≈436 mAh·g^{-1} at 5 A·g^{-1} with excellent stability, demonstrating

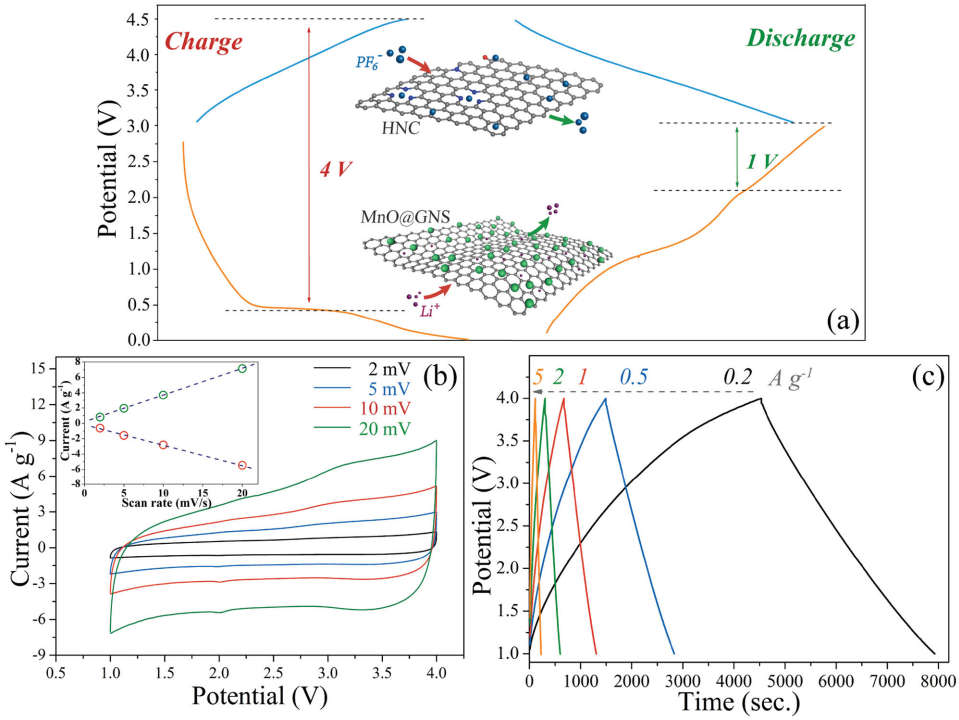

Figure 4. a) Voltage range illustration. b) CV curves of the full cells at different scan rates (inset: linear relationship between the redox peak current and scan rate). c) Typical charge–discharge plots of MnO@GNS//HNC devices.

superior performance indicators for both the capacity and rate capability in comparison to Li-insertion-type anodes (commonly 100–300 mAh·g^{-1} even at low current).[10,18] For bulk conversion reactions, poor electrical conductivity and cycling-induced agglomeration always hinder a high-rate capability and a stable cycle performance.[6] Figure S12 of the Supporting Information demonstrates that the electrode maintains an intact structure on both the macro- and microscale without any sign of pulverization. Therefore, the 5-nm nanometer-sized MnO crystals with highly flexible graphene bring robustness as well as ion and electron transport to every active site, which establish favorable bases and especially fast kinetics for higher energy and power density of Li-HSCs.

The CV curves of HNC electrodes reveal quasi-rectangular shapes with slight humps at all scan rates, indicating major EDLC and subordinate pseudo-capacitor behavior (Figure 3d). The minor faradic capacitance can be ascribed to storage induced by heteroatom-containing groups, appearing at ≈3.5 and 3.9 V for cathodic and anodic scan, respectively.[11] Figure 3e shows the contrast between HNC and commercial AC samples at low current, wherein the capacity of HNC (62 mAh·g^{-1}) is almost double that of AC (38 mAh·g^{-1}). While under higher rates, HNC exhibits excellent performance with high capacitance retention (≈63% from 0.2 to 5 A·g^{-1}, Figure 3f). Particularly, it shows similar climbing capacitance to MnO@GNS with negligible capacity loss under high current densities above 1 A·g^{-1} (as shown in Figure S10b, Supporting Information), which may be ascribed to the activation process of the functionalized carbon at high currents.[40] Different N-doped samples were utilized to highlight the positive effect of hierarchical porosity and abundant heteroatom-functionalities, wherein such porosity largely improved the rate performance while N doping along with high surface area boosted the capacitance (details in Table S1 and Figure S13 of the Supporting Information). Generally, the multi-type open pores form interconnected channels for facile ionic migration, and heteroatom species doped in the large external surface bring fascinating pseudo-capacitance with more active sites for fast electrostatic/chemical charge storage.[15,26]

Li-ion hybrid supercapacitors in which asymmetric assembly is employed could attain high-voltage performances, pushing energy and power density of the devices to a high level. A prelithiated MnO@GNS anode is capable of keeping the anodic potential as low as the lithiation plateau, thus achieving a high operation voltage in the cell.[41] Hence, the MnO@GNS anode is pre-lithiated to reach the main insertion voltage (≈0.45 V) and the HNC pair (3–4.5 V) provide the Li-HSC cell with a high voltage of 4 V. As illustrated in **Figure 4**a, the Li-MnO@GNS//HNC device with the typical hybrid mechanism could achieve an expansive potential range from 1 to 4 V by utilizing the lower voltage features of anodes. The CV curves of the overall hybrid cell show the near-rectangular shapes of the electrochemical capacitors, indicating interfacial electrochemical reactions with fast energy-storage kinetics (Figure 4b). A pair of slight humps revealed during all scan rates demonstrates pseudo-capacitance behavior at the lithiation/delithiation plateau of MnO, which corresponds to the voltage curves in the same image. The linear relationship between the redox peak current and the scan rate further confirms that the electrochemical reactions are not diffusion-limited but confined to the surface (inset of Figure 4b), which confirms that the improvement originates from the enhanced exterior-surface-charge storage.[40] Representative charge–discharge

curves are displayed in Figure 4c, demonstrating a near-linear correlation of ideal capacitor performance without diffusion limitation. Moreover, the negligible *IR* drops indicate excellent electrical conductivity, which is attributed to the 3D conductive matrices engaged in both the HNC cathode and MnO@GNS anode. The MnO@GNS//HNC device delivers a superb capacitance of ≈244 $F \cdot g^{-1}$ at a current density of 0.2 $A \cdot g^{-1}$ and keeps a high retention of ≈66% even when an extremely large current of 40 $A \cdot g^{-1}$ is applied, showing the excellent rate capability and high capacitance. Figure S14 of the Supporting Information shows that this cell represents a significant improvement over MnO@GNS//AC cells, proving the notable componential advantages and structural merits of the as-prepared material pair. In particular, owing to both electrode materials with 3D architectures composed of nanometer-sized constitutional units, the hybrid device reveals superior power stability with a slight decrease of capacitance above 10 $A \cdot g^{-1}$, demonstrating the fast energy-storage performances of hybrid supercapacitors.

As mentioned before, single electrode measurements show that both MnO@GNS and HNC electrodes deliver a rising capacity due to their textural features of low-valence Mn and heteroatom doping, respectively. When concurrently assembled into Li-HSCs, such a favorable material pair also bestows the device unique properties such as an ascending capacitance-during the initial ~400 cycles (**Figure 5**a, details in Figure S15, Supporting Information), revealing their synergy with respect to the overall performance. A capacitance retention of 81% was achieved after 2000 cycles, and the hybrid cell showed a favorable cyclic stability at a rapid 5 $A \cdot g^{-1}$, and could maintain up to 3000 cycles (at 76% retention) as well as good Coulombic efficiency (Figure S16, Supporting Information). Furthermore, the charge–discharge processes are well contained within 1 to 4 V without the detection of distortion (inset of Figure 5a). Generally, most earlier reports focused on one side of Li-ion hybrid cells to improve the overall performance. However, as an integrated system, it is of great significance to manipulate both LIB-type anodes and capacitor-type cathodes to overcome the intrinsic kinetics and capacity mismatch. As demonstrated with this compatible Li-HSC in this study, 5-nm MnO particles with a large surface fraction for Li storage and 3D HNC incorporating pseudocapacitive properties can effectively solve this problem.[25,34] Enhanced exterior electrochemical reactions in both interconnected porous structures successfully facilitate fast dynamics and also abundant energy storage.

As expected, this hybrid system achieves a high-level energy density of 127 $Wh \cdot kg^{-1}_{electrodes}$ (volumetric energy density: 121.8 $Wh \cdot L^{-1}$) at 125 $W \cdot kg^{-1}$ (119.8 $W \cdot L^{-1}$), which is calculated from the active materials in both electrodes (Figure S17a,b of the Supporting Information). Even at an ultrahigh power density of 25 $kW \cdot kg^{-1}$ (24 $kW \cdot L^{-1}$), which is beyond the recommended target for electric vehicles (15 $kW \cdot kg^{-1}$),[18] our hybrid system still retains an energy density of 83.25 $Wh \cdot kg^{-1}_{electrodes}$ (79.8 $Wh \cdot L^{-1}$), demonstrating its exceptional power delivery, i.e., almost ten-fold of what is reported for most Li-ion capacitors under similar conditions (Figure 5b, volumetric data in Figure S17c of the Supporting Information).[42,43] It is instructive to compare the MnO@GNS//HNC cell with many excellent reported Li-ion capacitors to clarify the power preponderance of the proposed

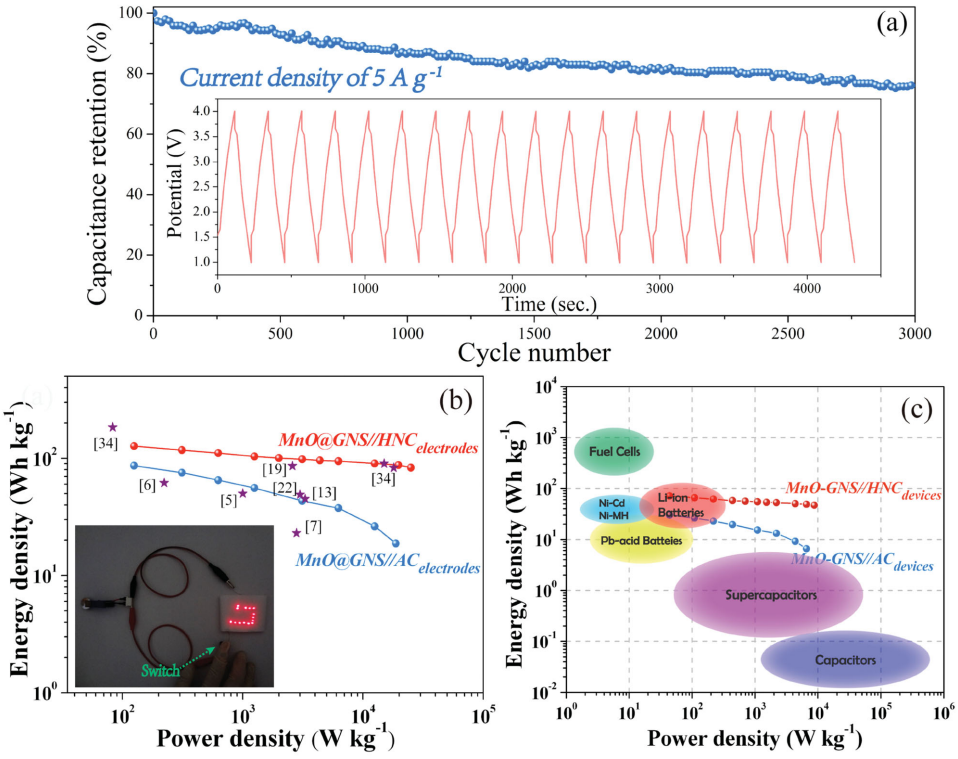

Figure 5. a) Long-term cycle performance and b) Ragone plots of MnO@GNS//HNC cells in comparison to the MnO@GNS//AC system and other selected representative data from the literature for Li-HECs. The inset in panel (b) shows the LED lighting application. c) Device-based performance for the currently available energy-storage systems.

design.[5,6,22,34] Although those reports showed favorable performances for common systems, such as TiO_2-B//AC,[7] $Li_4Ti_5O_{12}$//RGO,[13] and Fe_3O_4/graphene//graphene,[19] the hybrid device presented here manifests the most promising power delivery due to the successful remedy of mismatched kinetics. As the electrode materials account for 30–40% of the total package,[19,44] the entire Li–HSC package is expected to achieve a LIB-level energy density while upholding a capacitor-level power delivery (Figure 5c), and demonstrating a level course in the Ragone plot with high energy–power integration to bridge the gap between these systems. For instance, the energy density reaches up to 50 $W \cdot h \cdot kg^{-1}_{package}$ at a packaged power of 4 $kW \cdot kg^{-1}_{package}$ (based on the total package). Finally, we evaluated a light-emitting diode (LED) system to further test the performance of our system in tentative applications. After fast charging, a single 4 V hybrid cell could drive 14 LEDs forming a "Li" pattern for over 2 min (inset of Figure 5b, and Figure S18 of the Supporting Information), which signifies a high-voltage output and also indicates the potential of Li–HSCs for future practical applications.

In summary, a couple of hierarchical 3D materials were fabricated with a simple method and simultaneously employed in Li-ion hybrid supercapacitors. The MnO@GNS anode was subtly controlled down to the 5-nm scale to achieve a large exposed exterior surface and remitting diffusion-controlled lithiation/delithiation processes. In addition, the hierarchical porous texture and N-decoration of HNC improved the supercapacitive performance enormously, with ultrathin carbon sheets ensuring a large external active surface and high electrical conductivity. Benefiting from such a coherent design to achieve rapid electrochemical kinetics, the hybrid device demonstrated a superior energy output and even better power delivery in comparison to previous unilaterally designed systems, revealing the effective remedy of common challenges on mechanism-induced electrode mismatches. These high-voltage devices with a combination of high energy and power performance bridge the gap between batteries and supercapacitors, and represent a significant step forward. This simultaneous manipulation of hierarchical 3D structures signifies an advanced technology for fabricating sophisticated Li-ion hybrid devices, and can be regarded as a general model for energy storage with a high power demand.

Experimental Section

Synthesis of MnO@GNS: Graphene was synthesized by using the modified Hummers method from graphite, followed by thermal reduction. To prepare MnO@GNS composites, graphene (30 mg) was dissolved in ethylene glycol (30 mL) under vigorous stirring. Then, 0.142 g $KMnO_4$ and 0.75 g urea were added under 20 min of stirring and 30 min of ultrasonic treatment. The mixture was transferred into a 50 mL Teflon-lined stainless steel autoclave and then heated at 200 °C in an oven for 1 h. The resulting precipitate was harvested by centrifuging with distilled water repeatedly, followed by drying in vacuum at 80 °C overnight. The sample was finally sintered at 600 °C under Ar atmosphere for 4 h at a heating rate of 5 $°C \cdot min^{-1}$.

Synthesis of HNC: Urea and glucose with a mass ratio of 10:1 were dissolved in a mixed solution (distilled water and ethanol 1:3, v/v). The mixed solution was first volatilized under moderate agitation constantly at 75 °C. The as-obtained sol was dried in an oven overnight. Finally, the mixture was subjected to pre-carbonization at 300 °C for 4 h and then kept at 950 °C for 10 h, with a heating rate of 5 $°C \cdot min^{-1}$ under Ar atmosphere.

Materials Characterization: The prepared samples were characterized with XRD (Rigaku MiniFlex II diffractometer with Cu Kα radiation, λ = 1.5418 Å), SEM (Hitachi S-3500N), and HRTEM (FEI Tecnai G2F-20) featured with STEM. The samples were also characterized with elemental analysis (EA, vario EL CUBE), TG-DTA (Rigaku PTC-10A TG-DTA analyzer), XPS (Axis Ultra DLD, Kratos Analytical), nitrogen adsorption-desorption isotherms (Micromeritics ASAP 2020), and Raman spectroscopy (Renishaw inVia spectrometer, 514.5 nm Ar^+ laser).

Fabrication of the Half Cells: In a typical electrode preparation, active materials, conductive carbon black (Super P), and poly(vinylidene fluoride) (PVDF) were mixed in a ratio of 75:15:10 to form a slurry, and were then pasted on the current collectors (Cu foils for the MnO@GNS anodes and Al foils for the HNC cathodes). The typical mass loading was 1.2 and 3 $mg \cdot cm^{-3}$, and the corresponding thickness was 8.2 and 35 μm for the anode and cathode, respectively (Figure S17, Supporting Information). Electrochemical performances were evaluated in CR2025-type coin cells assembled in an argon-filled glove box. Lithium served as counter and reference electrodes. The electrolyte comprised of a solution of 1 M $LiPF_6$ in dimethyl carbonate (DMC)/ethyl methyl carbonate (EMC)/ethylene carbonate (EC) mixture (1:1:1 v/v/v), with a Celgard 2400 membrane as the separator. Galvanostatic charge–discharge tests were performed on a Land CT2001 battery tester. CV measurements were conducted on an electrochemical workstation (Zahner-Elektrik IM6e).

Fabrication of Hybrid Devices: Li–HSCs were also assembled in coin cells with pre-lithiated MnO@GNS composite as the anode, HNC material as the cathode, and Celgard 2400 membrane as the separator. During the prelithiation process, the anode was directly contacted with the Li metal with one drop of electrolyte between them, which lasted 1.5 h. The lithiated degree was estimated as 45%, calculated from the discharge capacity after prelithiation. Then, the anode was washed with dimethyl carbonate (DMC) and subjected to the assembly of coin cell-type Li-HSCs. The applied electrolyte was the same as that in half cells. Specific capacitances (C, $F \cdot g^{-1}$), energy density (E, $Wh \cdot kg^{-1}$) and power density (P, $W \cdot kg^{-1}$) were calculated through generally adopted equations:

$$P = \Delta V \times i / m$$

$$E = P \times t / 3600$$

$$\Delta V = (V_{max} + V_{min}) / 2$$

In the above equations, i (A), m (g), and t (s) denote the discharge current, mass of active materials, and discharge time, respectively. V_{min} (V) and V_{max} are the minimum and maximum working voltage during the charge-discharge process, respectively. The volumetric energy density is based on the thickness and mass loading following the equation: $\rho = m/Sd$, where m is the mass of electrode materials (g), S and d are the area (cm^2) and thickness (cm) of the effective electrode materials, respectively. The packing density of the cathode and anode was calculated as ~0.86 and 1.46 $g \cdot cm^{-3}$, respectively.

Supporting Information

Supporting Information is available from the Wiley Online Library or from the author.

Acknowledgements

Authors M.Y. and Y.Z. contributed equally to this work. This work was supported by NSFC (21273118 and 21421001) and MOE Innovation Team (IRT13022) in China.

Received: March 17, 2015
Revised: May 24, 2015
Published online:

[1] P. Simon, Y. Gogotsi, *Nat. Mater.* **2008**, *7*, 845.
[2] M. Armand, J. M. Tarascon, *Nature* **2008**, *451*, 652.
[3] A. S. Arico, P. Bruce, B. Scrosati, J. M. Tarascon, W. van Schalkwijk, *Nat. Mater.* **2005**, *4*, 366.
[4] K. Naoi, W. Naoi, S. Aoyagi, J. Miyamoto, T. Kamino, *Acc. Chem. Res.* **2013**, *46*, 1075.
[5] A. Jain, V. Aravindan, S. Jayaraman, P. S. Kumar, R. Balasubramanian, S. Ramakrishna, S. Madhavi, M. P. Srinivasan, *Sci. Rep.* **2013**, *3*, 3002.
[6] J. J. Ren, L. W. Su, X. Qin, M. Yang, J. P. Wei, Z. Zhou, P. W. Shen, *J. Power Sources* **2014**, *264*, 108.
[7] V. Aravindan, N. Shubha, W. C. Ling, S. Madhavi, *J. Mater. Chem. A* **2013**, *1*, 6145.
[8] H. Kim, M.-Y. Cho, M.-H. Kim, K.-Y. Park, H. Gwon, Y. Lee, K. C. Roh, K. Kang, *Adv. Energy Mater.* **2013**, *3*, 1500.
[9] Q. Wang, Z. H. Wen, J. H. Li, *Adv. Funct. Mater.* **2006**, *16*, 2141.
[10] K. Leng, F. Zhang, L. Zhang, T. Zhang, Y. Wu, Y. Lu, Y. Huang, Y. Chen, *Nano Res.* **2013**, *6*, 581.
[11] A. Vlad, N. Singh, J. Rolland, S. Melinte, P. M. Ajayan, J. F. Gohy, *Sci. Rep.* **2014**, *4*, 4315.
[12] M. Yang, Y. Zhong, X. Zhou, J. Ren, L. Su, J. Wei, Z. Zhou, *J. Mater. Chem. A* **2014**, *2*, 12519.
[13] V. Aravindan, D. Mhamane, W. C. Ling, S. Ogale, S. Madhavi, *ChemSusChem* **2013**, *6*, 2240.
[14] M. Yang, Y. Zhong, L. Su, J. Wei, Z. Zhou, *Chem. Eur. J.* **2014**, *20*, 5046.
[15] X. Zhuang, F. Zhang, D. Wu, X. Feng, *Adv. Mater.* **2014**, *26*, 3081.
[16] B. E. Conway, *J. Electrochem. Soc.* **1991**, *138*, 1539.
[17] V. Augustyn, P. Simon, B. Dunn, *Energy Environ. Sci.* **2014**, *7*, 1597.
[18] V. Aravindan, J. Gnanaraj, Y. S. Lee, S. Madhavi, *Chem. Rev.* **2014**, *114*, 11619.
[19] F. Zhang, T. Zhang, X. Yang, L. Zhang, K. Leng, Y. Huang, Y. Chen, *Energy Environ. Sci.* **2013**, *6*, 1623.
[20] Y. Zhong, L. Su, M. Yang, J. Wei, Z. Zhou, *ACS Appl. Mater. Interfaces* **2013**, *5*, 11212.
[21] H. Jiang, Y. Hu, S. Guo, C. Yan, P. S. Lee, C. Li, *ACS Nano* **2014**, *8*, 6038.
[22] K. Karthikeyan, S. Amaresh, V. Aravindan, H. Kim, K. S. Kang, Y. S. Lee, *J. Mater. Chem. A* **2013**, *1*, 707.
[23] F. Beguin, V. Presser, A. Balducci, E. Frackowiak, *Adv. Mater.* **2014**, *26*, 2219.
[24] C. R. Pérez, S.-H. Yeon, J. Ségalini, V. Presser, P.-L. Taberna, P. Simon, Y. Gogotsi, *Adv. Funct. Mater.* **2013**, *23*, 1081.
[25] P. Simon, Y. Gogotsi, B. Dunn, *Science* **2014**, *343*, 1210.
[26] H. Jiang, P. S. Lee, C. Li, *Energy Environ. Sci.* **2013**, *6*, 41.
[27] A. C. Ferrari, D. M. Basko, *Nat. Nanotechnol.* **2013**, *8*, 235.
[28] Z.-S. Wu, G. Zhou, L.-C. Yin, W. Ren, F. Li, H.-M. Cheng, *Nano Energy* **2012**, *1*, 107.
[29] H. Wang, H. Dai, *Chem. Soc. Rev.* **2013**, *42*, 3088.
[30] Z. Li, Z. Xu, X. Tan, H. Wang, C. M. B. Holt, T. Stephenson, B. C. Olsen, D. Mitlin, *Energy Environ. Sci.* **2013**, *6*, 871.
[31] Y. Mao, H. Duan, B. Xu, L. Zhang, Y. Hu, C. Zhao, Z. Wang, L. Chen, Y. Yang, *Energy Environ. Sci.* **2012**, *5*, 7950.
[32] Y. Zhong, M. Yang, X. Zhou, J. Wei, Z. Zhou, *Part. Part. Syst. Charact.* **2015**, *32*, 104.
[33] E. Lim, H. Kim, C. Jo, J. Chun, K. Ku, S. Kim, H. I. Lee, I. S. Nam, S. Yoon, K. Kang, J. Lee, *ACS Nano* **2014**, *8*, 8968.
[34] H. Wang, Z. Xu, Z. Li, K. Cui, J. Ding, A. Kohandehghan, X. Tan, B. Zahiri, B. C. Olsen, C. M. Holt, D. Mitlin, *Nano. Lett.* **2014**, *14*, 1987.
[35] M. Yang, Y. R. Zhong, X. L. Zhou, J. J. Ren, L. W. Su, J. P. Wei, Z. Zhou, *J. Mater. Chem. A* **2014**, *2*, 12519.
[36] Y. G. Zhu, Y. Wang, Y. M. Shi, Z. X. Huang, L. Fu, H. Y. Yang, *Adv. Energy Mater.* **2014**, *4*, 1301788.
[37] J. Yan, L. P. Yang, M. Q. Cui, X. Wang, K. J. J. Z. Chee, V. C. Nguyen, V. Kumar, A. Sumboja, M. Wang, P. S. Lee, *Adv. Energy Mater.* **2014**, *4*, 1400781.
[38] Y. Sun, X. Hu, W. Luo, F. Xia, Y. Huang, *Adv. Funct. Mater.* **2013**, *23*, 2436.
[39] J. Yue, X. Gu, L. Chen, N. Wang, X. Jiang, H. Xu, J. Yang, Y. Qian, *J. Mater. Chem. A* **2014**, *2*, 17421.
[40] H. Kim, K. Y. Park, J. Hong, K. Kang, *Sci. Rep.* **2014**, *4*, 5278.
[41] M. Kim, F. Xu, J. H. Lee, C. Jung, S. M. Hong, Q. M. Zhang, C. M. Koo, *J. Mater. Chem. A* **2014**, *2*, 10029.
[42] V. Aravindan, Y. L. Cheah, W. F. Mak, G. Wee, B. V. R. Chowdari, S. Madhavi, *ChemPlusChem* **2012**, *77*, 570.
[43] V. Aravindan, N. Shubha, W. C. Ling, S. Madhavi, *J. Mater. Chem. A* **2013**, *1*, 6145.
[44] Y. Gogotsi, P. Simon, *Science* **2011**, *334*, 917.